



Simulation and Fabrication of Stronger, Larger, and Faster Walking Biohybrid Machines

Gelson J. Pagan-Diaz, Xiaotian Zhang, Lauren Grant, Yongdeok Kim, Onur Aydin, Caroline Cvetkovic, Eunkyoung Ko, Emilia Solomon, Jennifer Hollis, Hyunjoon Kong, Taher Saif, Mattia Gazzola, and Rashid Bashir*

Advancing biologically driven soft robotics and actuators will involve employing different scaffold geometries and cellular constructs to enable a controllable emergence for increased production of force. By using hydrogel scaffolds and muscle tissue, soft biological robotic actuators that are capable of motility have been successfully engineered with varying morphologies. Having the flexibility of altering geometry while ensuring tissue viability can enable advancing functional output from these machines through the implementation of new construction concepts and fabrication approaches. This study reports a forward engineering approach to computationally design the next generation of biological machines via direct numerical simulations. This was subsequently followed by fabrication and characterization of high force producing biological machines. These biological machines show millinewton forces capable of driving locomotion at speeds above 0.5 mm s^{-1} . It is important to note that these results are predicted by computational simulations, ultimately showing excellent agreement of the predictive models and experimental results, further providing the ability to forward design future generations of these biological machines. This study aims to develop the building blocks and modular technologies capable of scaling force and complexity of these devices for applications toward solving real world problems in medicine, environment, and manufacturing.

required to perform design troubleshooting. This points to a necessity of improving upon the method of designing function-specific biological machines. These soft robots primarily consist of actuating cells, such as cardiac or skeletal muscle cells, within or around a hydrogel which permits the differentiation and maturation of these cells while providing structural and physical cues for the formation of functional (i.e., contracting) tissue.^[3,9–12] The scaffolds provide the “form” and are used to convert the “function” from the tissue into a controlled output, for example, some manner of locomotion such as swimming or walking.^[1,4–6,13] These scaffolds can be highly customizable through development of 3D printing techniques such as stereolithography, which permit these biological machines to have multiple shapes, and applicable to numerous muscle tissue geometries and functional outputs.^[9,11,12,14,15] Despite this design flexibility, in order to achieve effective forward engineering of biological machines with targeted performance, a critical necessity is the ability to model the interaction between the contractile tissue and its interaction with the actuating scaffold to predict its functional output.

One key factor in order to achieve ground up engineering of new biohybrid systems is to analytically characterize new design parameters in order to expand the breadth of possible

1. Introduction

While engineering biohybrid robots that utilize hydrogels as biomaterials and biocompatible scaffolds has become a growing field in the last decade, the design approaches have been mostly attempted by trial and error.^[1–8] This can be particularly disadvantageous considering the large amount of time and resources

G. J. Pagan-Diaz, L. Grant, Dr. C. Cvetkovic,^[+] E. Ko
 Department of Bioengineering
 University of Illinois
 Urbana-Champaign, Urbana, IL 61801, USA
 X. Zhang, O. Aydin, Prof. T. Saif, Prof. M. Gazzola
 Department of Mechanical Science and Engineering
 University of Illinois
 Urbana-Champaign, Urbana, IL 61801, USA
 Y. Kim
 Department of Material Science and Engineering
 University of Illinois
 Urbana-Champaign, Urbana, IL 61801, USA

^[+]Present address: Houston Methodist Research Institute, Houston, TX 77030, USA

DOI: 10.1002/adfm.201801145

Prof. H. J. Kong
 Department of Chemical and Biomolecular Engineering
 University of Illinois
 Urbana-Champaign, Urbana, IL 61801, USA
 Dr. E. Solomon, Dr. J. Hollis
 Bioscience Division
 Los Alamos National Laboratory
 Los Alamos, NM 87545, USA
 Prof. M. Gazzola
 National Center for Supercomputing Applications
 University of Illinois
 Urbana-Champaign, Urbana, IL 61801, USA
 Prof. R. Bashir
 Department of Bioengineering and Carle Illinois College of Medicine
 University of Illinois
 Urbana-Champaign, Urbana, IL 61801, USA
 E-mail: rbashir@illinois.edu

applications. The goal is to design these biological machines with a high degree of control, tissue-to-scaffold dynamics, and longevity, among other parameters. Such advances include the use of light to temporally control muscle contractions, micropatterning to achieve spatial coordination of contraction, and incorporation of biomolecules to control the degradation of the structural matrix.^[16–18]

Force generation to drive actuation is one of the most critical parameters in engineering of skeletal muscle tissue constructs. Being able to scale up the force would enable the formation of larger or more complex systems, as well as adding new levels of functionality. Currently, the largest force achieved in biohybrid tissues has been reported to be 1.18 mN, with a structure of four stacks of cardiac $1.16 \pm 0.08 \text{ cm}^2$ 2D sheets of thickness of $45 \pm 8 \mu\text{m}$.^[19] However, this was achieved on a fixed scaffold. While untethered biological machines have been designed to walk, their current force per stroke during external stimulation was 200 μN for a design with a largest dimension of 6 mm.^[20] There are many biological factors that affect force generation in myogenic tissue, such as the cell source or biomolecular pathways that regulate the metabolism, or differentiation of the myofiber type.^[21] However, these are hard to control and often require a complex regulation of gene expression.^[22,23] Another approach would be to have the biohybrid material respond to environmental cues that can be directly engineered. A number of studies have employed exercising the muscle during maturation through a series of mechanical stretches or electrical stimulations and have shown greater than twofold increase in force generation postexercising regimens.^[24–26]

In the present work, we expand upon our prior walker biorobot (biobot) design by developing a new tissue fabrication protocol that increases the force per single actuator by generating longer myotubes (MT) and proposing a mathematical model to develop a predictive computer simulation based on empirically calculated force parameters characteristic to the biohybrid tissue (Figure 1). Our model is based on assemblies of Casserat rods, i.e., slender, soft, and shearable elements.^[27] By varying mechanical properties and by enabling contractile stresses, we can model both scaffold and living tissue as well as their dynamic interactions. Once calibrated with experimental data, we employed these simulations to effectively modify the tissue morphology and contractile characteristics

of these biological machines to pointedly scale the force to a higher range than has been previously reported, in order to power the actuation centimeter-scale skeleton structure (two times larger than prior design). Specifically, a larger number of single actuators was achieved by increasing the tissue volume while controlling tissue thickness to avoid limitations of nutrient-diffusion and a larger, stiffer scaffold was designed to maintain functionality of the biobot driven by a higher-force generating muscle tissue, as previous designs would collapse under the larger force. Finally, critical factors are further quantified to revise computational models. By implementing this new modeling approach, we could predict and validate designs, thus enhancing the efficiency of forward engineering these biohybrid systems and serve as new design tools to successfully develop the next generation of biohybrid robots from the ground up.

2. Results and Discussion

2.1. Formation of Biological Machines through Critical Design Parameters

The design of the walker biobot consists of two pillars, or legs, connected by a beam. Differentiated muscle tissue is held between the two legs and as it contracts, it exerts force on these legs causing the flexible beam to bend. As the beam deforms, the tips of the pillars come close to each other and as the muscle relaxes so does the beam, returning the pillars to their original position. This muscle–pillar–beam design mimics the muscle–tendon–bone relationship found in vivo. The skeleton structure of the biobot is fabricated by using a modified stereolithography apparatus (SLA) to 3D print a poly(ethylene glycol) diacrylate (PEGDA) hydrogel from a computer aided design tool (Figure 2a). The biohybrid tissue is then engineered by mixing a suspension of C2C12 mouse skeletal myoblasts (MB) with extracellular matrix (ECM) proteins fibrinogen and thrombin, and injecting the mixture into a 3D printed PEGDA mold, to allow for gelation (Figure 2b). This results in cells engrafted in a web-like fibrin hydrogel (Figure 2c).^[28] The cell-laden gel subsequently compacts, and compaction is restricted by the stiff PEGDA mold, inducing tension across the fibrin gel, which

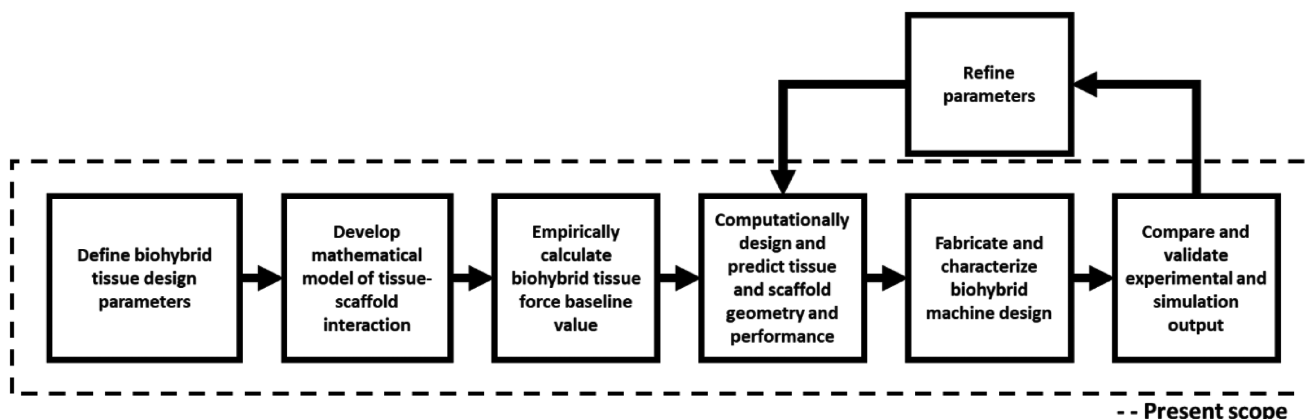


Figure 1. Process flow for the development of a computational predictive model for targeted forward engineering of biohybrid actuators.

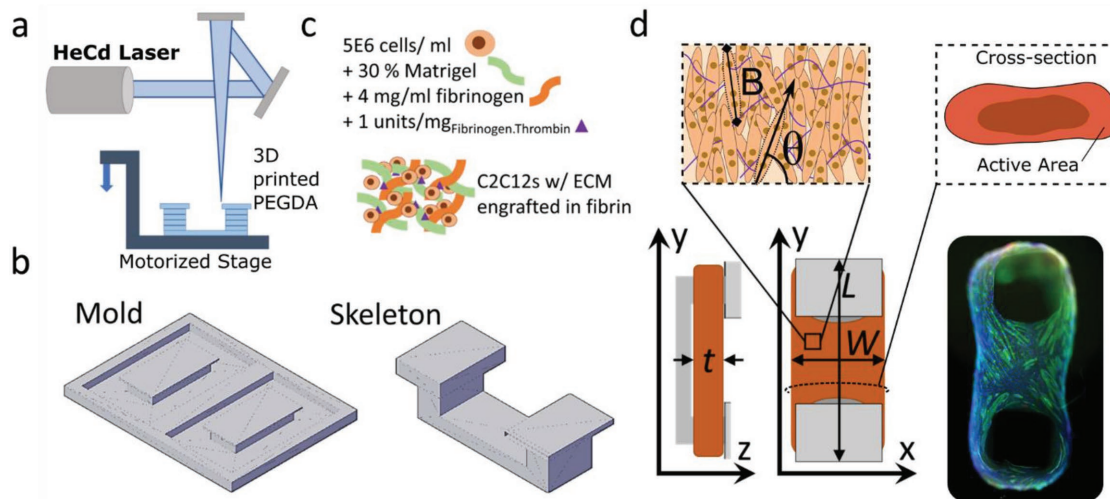


Figure 2. Design parameters of skeletal muscle biological machine. a) 3D stereolithography apparatus was used to 3D print PEGDA resin into the molding and skeleton structures, b) in order to guide the formation of muscle tissue and translate muscle contraction to locomotion, respectively. c) Biohybrid tissue is formed by mixing C2C12 myoblasts with ECM proteins. d) Forward engineering of muscle design for next generation biobots can be modeled as a function of muscle geometry of active tissue, and actuator length and alignment. (L : length, W : width, t : thickness, θ : myotube alignment, B : myotube length and active area).

serves as a mechanical cue to direct the aligned differentiation of myotubes. Differentiated muscle can then be electrically stimulated to contract cyclically, which elicits locomotion by a two-anchor gait.

Force production and functional output can be further engineered by visualizing the muscle tissue as a series of actuators (i.e., myotubes) bound together by an inert hydrogel, and addressing the geometrical parameters (Figure 2d). The internal muscle contractile stresses may be modeled as

$$F_{\text{muscle}} = n * F_{\text{MT}}(B) * \sin(\theta_{\text{avg}}) = A_{\text{tol}} * \gamma * \sigma_{\text{MT}} * \sin(\theta_{\text{avg}}) \quad (1)$$

where F_{MT} and σ_{MT} are the contractile force and stress of individual myotubes, θ_{avg} is the mean angle of individual myotubes with respect to the lateral axis of skeleton actuation, A_{tol} is the cross-sectional area, and γ is the ratio of live actuating to necrotic tissue. From this relation, the net force of the contracting tissue is a function of the force production of individual myotubes, which has been shown to be proportional to myotube length, B .^[29] Thus, by increasing the number and length of myotubes, force can be linearly scaled up. This can be achieved by enlarging the tissue volume ($L \times W \times t$). However, there is a nutrient diffusion limitation of about 200 μm from the tissue surface, which caps the practical t that can be designed before cell death occurs and a necrotic core forms impeding further force production.^[30] Finally, Equation (1) implies that the net force for a given biohybrid muscle is maximized when all myotubes are aligned parallel to the direction of actuation. Given this, the output force at the pillars can be also expressed as $F = k(\Delta x)$, where k is the stiffness constant of the scaffold against which the tissue is contracting, and Δx is the displacement of the scaffold pillars. Hence, if the tissue size and resulting myotube force are increased, the scaffold also must be redesigned to avoid collapse of the scaffold.

2.2. Increasing Force Production of Individual Myofiber

The first parameter that was targeted was the myotube length, as that would increase the force baseline for any subsequent design of any given biohybrid actuator. To increase the length of myotubes, we added a differentiation step in 2D prior to suspension of the cells in the 3D fibrin hydrogel, as opposed to inducing differentiation of MB in 3D fibrin hydrogel (Figure S1a, Supporting Information). Substrate stiffness can profoundly affect myogenesis and longer myotubes can be obtained at surfaces of higher stiffness.^[31,32] Stiffness of fibrin gels formed using a fibrinogen concentration of 4 mg mL⁻¹ mixed with 1 unit mg⁻¹ fibrinogen is typically <1 kPa, which is much softer than polystyrene plastic ($\approx 10^6$ kPa).^[33] Therefore, myoblasts were differentiated in 2D polystyrene for 5 d until elongated MT were observed (Figure 3a) and maturation markers were shown to plateau (Figure S2, Supporting Information). Afterward, standard 3D seeding protocols were followed (See the Experimental Section).

After engraving myotubes in the 3D fibrin hydrogel, the biohybrid tissue showed no significant change in differentiation markers (Figure S3, Supporting Information) indicating that biohybrid tissue development mainly consisted of myotube alignment and remodeling of extracellular matrix. After two weeks of maturation, MT tissue showed analogous structural characteristics compared to MB tissue (Figure 3b; Figure S4, Supporting Information). However, within the muscle, individual myotubes showed a 1.5-fold increase in length for MT samples (Figure 3c; Figure S1b, Supporting Information) indicating a higher degree of myogenic differentiation, which is corroborated by a significant increase in fusion index (FI) and concentration of the muscle creatine kinase (MCK) (Figure S1c,d, Supporting Information).^[34] It is important to note that there was no significant change in viability as measured from the MTS assay

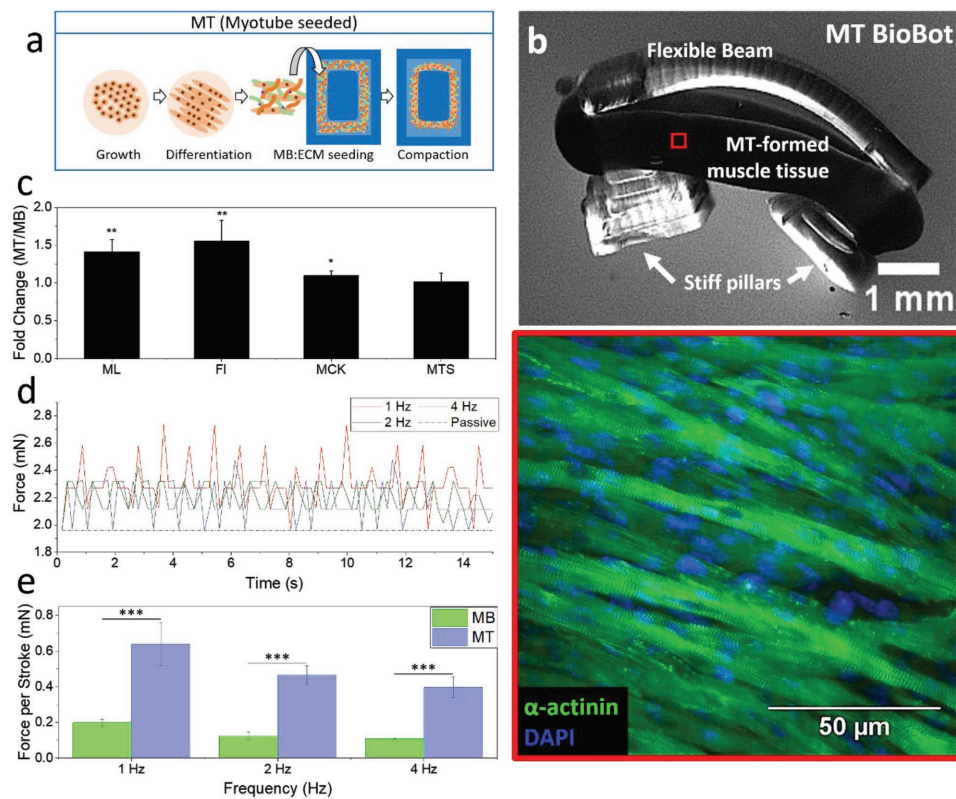


Figure 3. Increasing the force baseline by extending myotube length. a) Process flow diagram of muscle formation through seeding myotubes (MT). b) Stereoscopic image of an MT bot exerting passive force on PEGDA skeleton (scale bar: 1 mm). MT formed biobot consisting in striated biohybrid muscle in 3D. c) MT formed tissue was compared to myoblasts (MB) formed tissue through various parameters: (ML) myotube length (mean \pm SD, $n = 20$), (FI) fusion index—number of nuclei per multinucleated myotube—(mean \pm SD, $n = 20$), (MCK) muscle creatine kinase concentration (mean \pm SD, $n = 4$), and (MTS) cell viability (mean \pm SD, $n = 4$). d) Total force output of MT biobot for different frequencies of stimulation (0.5 Hz, 1 Hz, 2 Hz, and 4 Hz). e) Force per stroke at different stimulation frequencies (mean \pm SD, $n = 6$) (* $p < 0.05$, ** $p < 0.005$, *** $p < 0.0005$, T-test).

(3-(4,5-dimethylthiazol-2-yl)-5-(3-carboxymethoxyphenyl)-2-(4-sulfophenyl)-2H-tetrazolium) (MTS) between MT and MB tissue, indicating that changes in differentiation markers were not caused by increased cell numbers (Figure S1e, Supporting Information).

The resulting forces were then compared between the MB and MT tissue, by installing them into the untethered 3D PEGDA skeletons (Figures 2b and 3b). The force in these two constructs was correlated to the beam deflection using the Bernoulli–Euler model. After muscle maturation, the muscle develops a passive tension, which deflects the beam by a certain length. During electrical stimulation at constant frequency, both MB and MT bots showed cyclic contractions corresponding with the stimulation frequencies (Figure 3d; Figure S1f, Supporting Information). Moreover, MT bots showed a substantial force increase when electrically stimulated. The force elicited per stroke from the MB bots was consistent in magnitude to previously reported constructs.^[26] Contrastingly, the MT muscle tissue showed a threefold increase in force per stroke across different stimulation frequencies (Figure 3e). This indicated that the a priori differentiation of cells before they are integrated into the matrix results in increased myotube length leading to higher forces per stroke as expected.

2.3. Rod-Based Simulations for Design of Next Generation Biological Machines

In order to design a larger and stronger bot in a targeted fashion, we needed to optimize around both the biological and mechanical constraints. Aiming to effectively actuate on a skeleton structure 2x larger than previously reported walkers, a muscle structure capable of applying millinewton level forces was required.^[20] This required a larger muscle structure. One of the limitations of designing biological tissue with a larger geometric latitude is that the nutrient and waste diffusion will be hampered past the limit of about 200 μm .^[35] This will cause a necrotic core to form for cells farther than the diffusion distance, resulting in scar tissue and impeding the actuation and increase of force (Figure 2d). To overcome this, a mold was fabricated with a new design which was an integration of our prior muscle “strip” and muscle “ring” biobot design model (Figure 4a).^[6] This new design can be implemented for larger planar geometries, while avoiding the necrotic core by controlling the thickness of the actuating tissue and maintaining the modularity of the process to increase the design window. Following the MT tissue differentiation protocol explained in Figure 3, myotube/ECM solution was dispensed

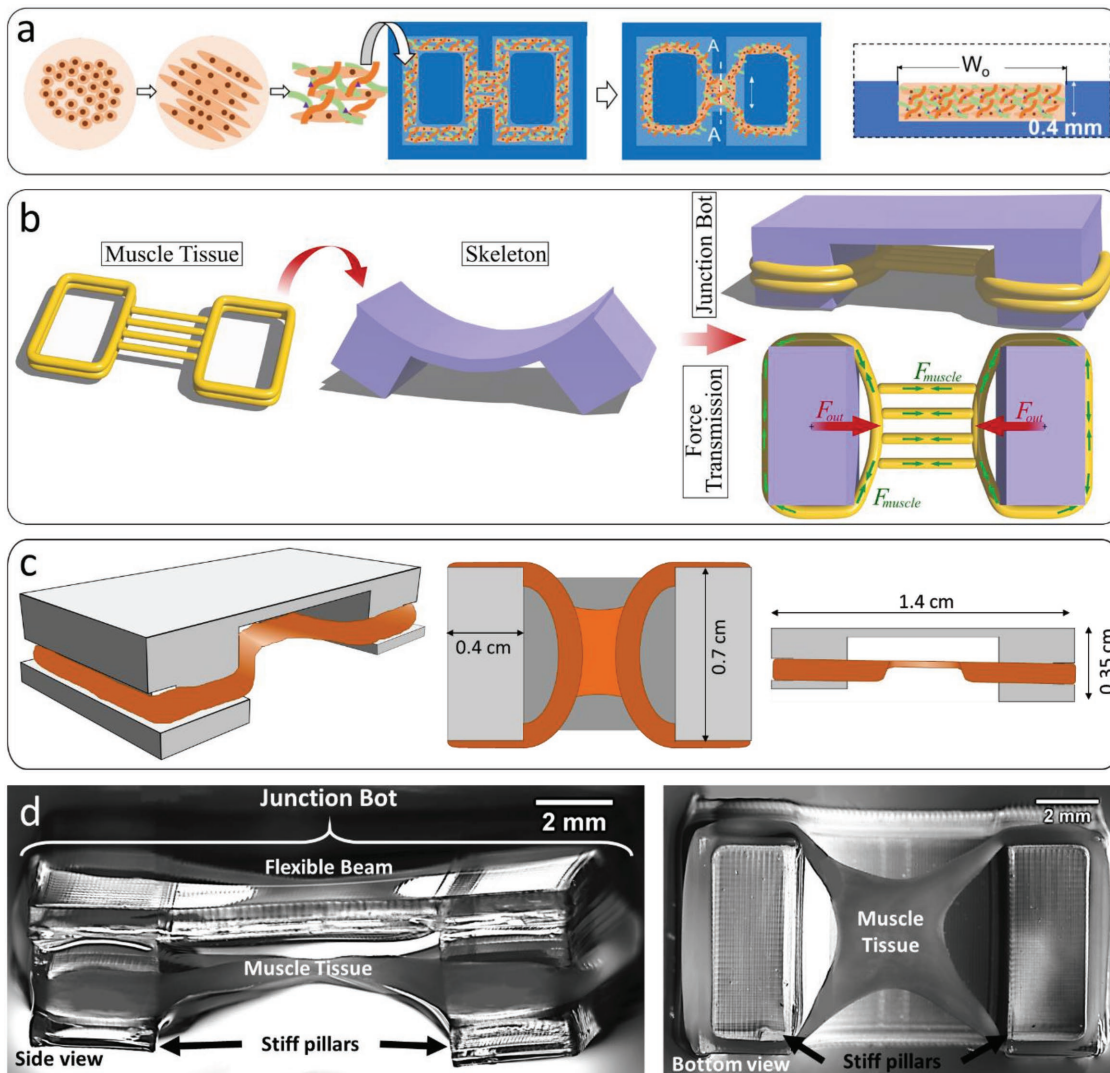


Figure 4. Formation of junction bot guided by rod-based simulations. a) Process flow diagram of myotube/gel solution seeding and tissue formation across a trench mold. b) Computational integration of muscle to designed skeleton to model the junction bot and study force transmission of the computational model. c) Representation of muscle tissue integrated onto a 3D printed PEGDA centimeter-scale skeleton (skeletons drawn to scale). d) (left) optical image angled side view of the entire junction biobot structure, (right) phase contrast image of mature junction biobot from the bottom side showing the muscle and the printed hydrogel scaffold.

on a mold with a shallow trench enabling the formation of a thin tissue region. This 400 μm deep trench would ensure that compacted tissue thickness was below the nutrient diffusion limit from either side.

This design was guided by the mechanical model of the muscle tissue, which was incorporated in a novel rod-based formalism for the simulation of arbitrary musculoskeletal structure (Note S1, Supporting Information). The simulation approach aimed to model both the skeleton of the bot and the muscle tissues, with the capacity of capturing the dynamic responses during beam deformation and muscle contraction. Assembling of the junction bot for simulation purposes consists in setting the force generation model of the skeletal muscle tissue (Figure 4b). Aiming to design biohybrid robots with arbitrary muscle arrangement and the structure of the skeleton, a general relationship was expanded from Equation (1)

between the stimulated muscular stress $\sigma_{\text{muscle}} = F_{\text{muscle}}/A_{\text{tol}}$ and force output to 3D scaffolds F_{out} , where A_{tol} is the overall cross-sectional area of the muscle. A force model was thus proposed, which involved the ratio of the area of active muscle cells $\gamma = A_{\text{act}}/A_{\text{tol}}$, and the average myotube alignment angle θ_{avg} . The relationship was defined as

$$F_{\text{out}} = A_{\text{tol}} \left(\gamma \sigma_{\text{muscle}} - \frac{E_{\text{muscle}} \epsilon}{1 - \epsilon} \right) \quad (2)$$

where E_{muscle} is the muscular Young's modulus and ϵ denotes the strain of the muscle tissue. The latter term conveys the axial rigidity and the radial deformative behavior of the muscle. Furthermore, the overall stress is comprised of the passive and active elements, formulated as $\sigma_{\text{muscle}} = \sigma_{\text{pas}} + \sigma_{\text{act}}$.

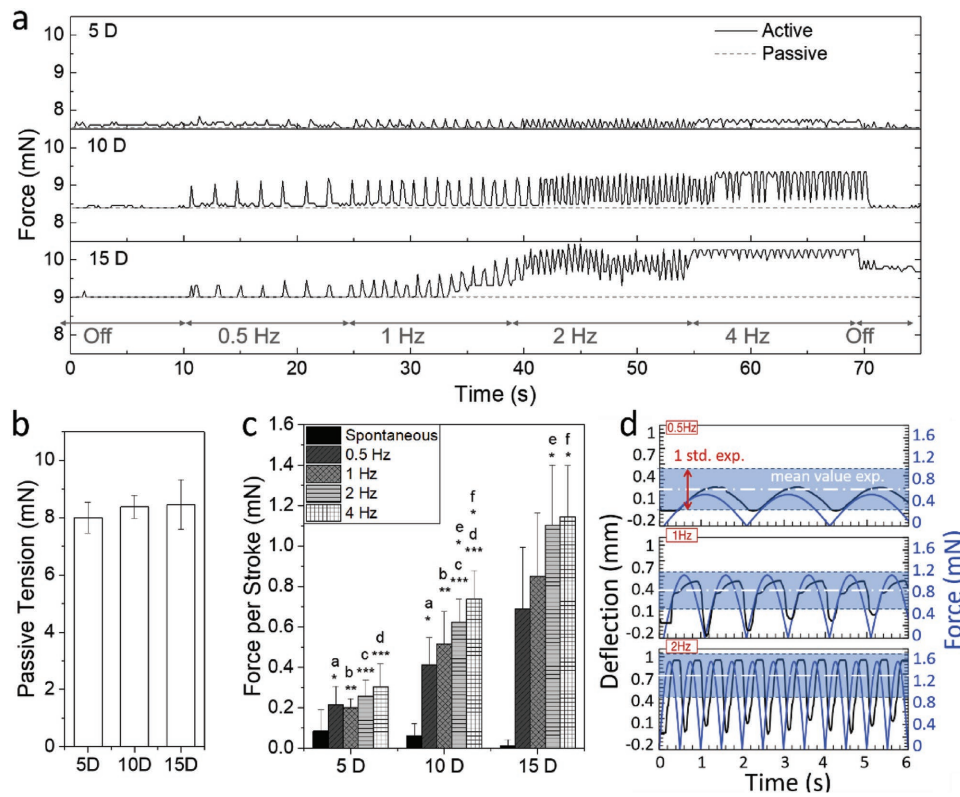


Figure 5. Force development of junction bot. a) Representative force (mN) response of muscle successively stimulated with an electrical field at increasing frequencies (0.5, 1, 2, 4 Hz) at 5 d (top), 10 d (middle), and 15 d (bottom) after seeding. b) Passive force at 5, 10, and 15 d of seeding (mean \pm SD, $n = 6$). c) Force response at different frequencies of stimulation for each day of stimulation (5, 10, and 15 d) (mean \pm SD, $n = 6$). d) Computationally calculated deflection of pillars (black) and resulting force (blue) simulated for 0.5, 1, and 2 Hz as predicted by the model, and falling within the 1 standard deviation of the empirical force of our bots at 15 D under respective frequencies of stimulation (* $p < 0.05$; ** $p < 0.005$; *** $p < 0.0005$, T-test).

In order to design a larger bot, or more general biohybrid bot with arbitrary configuration, σ_{muscle} has to be defined as the functional input. Here, σ_{muscle} is derived based on the force characterization of the MT bot, which has been demonstrated to have the desired force increase ($F_{\text{out}} = 2.6$ mN). Thus, following Equation (2) and given the geometrical parameters ($A_{\text{tol}} = 1.08 \text{ mm}^2$, $\gamma = 0.83$, $\theta_{\text{avg}} \approx 90^\circ$), we have $\sigma_{\text{muscle}} = 10.39 \text{ mN mm}^{-2}$. For the muscle arrangement of the new bot design, the same muscle stress is proposed to apply, since the same protocol is leveraged. It is also worth noticing that because of the thickness controlled design, $\gamma \approx 1$. Therefore from the muscle model, a muscle tissue with cross-sectional area around 1 mm^2 is expected to elicit forces $F_{\text{muscle}} > 10 \text{ mN}$.

A complementary skeleton structure was also computationally designed to handle these levels of force, and be capable of locomotion. The elastic modulus E of the PEGDA beam (see the Experimental Section, Equation (3)) was kept the same (319.4 kPa) as the small skeletons for ease of fabrication. However, in order to accommodate the expected increase in force, the stiffness constant was increased by increasing the moment of inertia by $\approx 5\times$ (small skeleton: 0.04 mm^4 ; large skeleton: 0.2 mm^4) by increasing the beam dimensions accordingly to also be suitable for the designed tissue (Figure S5, Supporting Information). By assembling the muscle tissue with the skeleton in simulation, the final configuration of the bot is shown in Figure 4b, with the passive muscle stress overcoming the

intrinsic bending stiffness of the skeleton. The simulation result reveals a 1.4 mN active force being applied on each pillar upon muscle stimulation, rendering a successful steady walking of the new bot (Movie S5, Supporting Information). The details of the simulation results are presented later with the experimental characterizations.

These calculations permitted the fabrication of a centimeter-scale asymmetric skeleton, unto which the designed muscle structure could be modularly installed (Figure 4c; Movie S1, Supporting Information).

Due to the formation of a thickness-controlled muscle region bridging the tissues that wrap around the pillars, this tissue structure was labeled “junction bot,” and for ease of discussion will be referred to as such (Figure 4d; Figure S6, Supporting Information).

2.4. Empirical Characterization of the Junction Bot

Once the junction bot design was successfully manufactured (Figure 4), it was confirmed that it could effectively elicit a macroscale deflection of the pillars when stimulated (Movie S2, Supporting Information). The samples were electrically stimulated at multiple frequencies at 5, 10, and 15 d (5 D, 10 D, and 15 D) after seeding (Figure 5a). As expected, 5D samples showed contraction force below 3% of the total force (active +

passive) calculated from the beam deflection. However, by 10 D and more so at 15 D, contraction force increased to 7.5% and 12.5% of the total achieved force. Passive tension did not significantly change during maturation, averaging around 7.99 ± 0.54 , 8.38 ± 0.40 , and 8.45 ± 0.86 mN for 5 D, 10 D, and 15 D, respectively (Figure 5b). Passive tension is produced by the protein titin spanning across the half-sarcomere.^[36] Therefore, the stable baseline in the passive force could be another indication that myotubes have reached steady state of differentiation prior to seeding. On the other hand, the active force per stroke increased significantly over time (Figure 5c). Rate of increase of active force from 10 D to 15 D was smaller compared to that from 5 D to 10 D, which could be interpreted as sign of plateauing of tissue maturation. At stimulation frequencies of 2 and 4 Hz, junction bots were able to elicit stroke forces in the ranges of 1.10 ± 0.30 and 1.14 ± 0.25 mN, respectively, which are almost 6x higher than what was previously achieved for these skeletal muscle actuated walking bio-bots.^[20] Furthermore, similar to native tissue, this engineered skeletal muscle exhibited a positive force–frequency relationship, notable at 10 D and 15 D.^[21] In addition, one standard deviation around the mean force per stroke at 15 D coincided with the calculated forces of 0.5, 1, and 1.4 mN as compared to the stimulation frequencies of 0.5, 1, and 2 Hz, respectively, and the resulting computed dynamic deflections of ≈ 0.3 , ≈ 0.5 , ≈ 1 mm, respectively (Figure 5d). This provided key confirmation that the muscle-scaffold model could serve as a predictive model for force output of engineered muscle tissue.

2.5. Empirical Effects of Geometrical Parameters on Force Output

Next, the junction geometry was examined as a parameter that could modulate force output. While dispensing myotube–ECM solution on the 3D molds, the solution entirely conformed to the mold dimensions followed by a compaction process as the fibrin hydrogel cross-links (Figure 6a). To quantify the relation between junction dimensions and force production, molds with trenches of initial seeding widths (W_0) of 3.5 mm ($W_{3.5}$), 7 mm (W_7), and 14 mm (W_{14}) were used to dispense myotube–ECM solution and then tested at 15 D (Figure 6b), at which final width had been reached (W_F). It was notable that the junction width did not compact linearly, relative to W_0 (Figure 6c). The interquartile range (IQR) of the W_F for $W_{3.5}$ junctions was between 2 and 3 mm, which corresponds to a ≈ 1.58 -fold compaction ratio. However, for W_{14} junctions, the IQR spanned ≈ 4 and 6 mm, corresponding to a compaction ratio of ≈ 3.08 -fold change. This relationship showed that the ratio by which these muscle junctions compacted was not constant (relative to W_0), but linearly correlated to the logarithm of W_0 , with a slope of 0.75 (Figure 6c, top). This was in fact unexpected and could have occurred in response to nonlinear dynamics between muscle cells and fibrin hydrogels, and that could be intriguing to further study in the future.

Nevertheless, the resulting force was discernably affected by W (Figure S7, Supporting Information). The passive tension significantly increased from 7.93 ± 0.3 mN for $W_{3.5}$, to 9.53 ± 0.68 mN for W_{14} , which constitutes on average

a 1.2-fold increase (Figure 6d). This effect from W_0 was far more perceivable in the force per stroke evoked during stimulation. However, this stimulated force exhibited a significant decrease for larger W_0 (Figure 6e). While junctions seeded at $W_{3.5}$ reached forces during strokes of 0.97 ± 0.27 mN, junctions of W_7 were significantly weaker with stroke forces of 0.67 ± 0.26 mN. This trend was even more extensive for W_{14} junctions, reaching relatively weak forces of 0.47 ± 0.17 mN. This negative force per stroke dependence to W_0 was hypothesized to be a result of a lack of myotube alignment for wider junctions. It is well documented that cells align parallel to a hydrogel matrix under a uniaxial tension, by responding to both mechanical and topographical cues.^[37,38] Given that all the muscle tissues were subjected to the same tensile resistance by the skeleton beam, narrower junctions would result in a more homogenous tension distribution and thus a more aligned cluster of myotubes, compared to wider junctions.^[39] This would then result in more force per stroke during stimulation, as expressed in Equation (1).

2.6. Empirical Effects of Myotube Alignment on Force Output

To quantify this force–myotube alignment relationship, fluorescence microscopy was used to compare alignment of populations of myotubes within the muscle junction of samples to the evoked force response measured prior to fixing samples for imaging (Figure 7a). Fluorescent images stained for the cellular membranes in the muscle junction were analyzed by ImageJ, where myotubes were detected as single elements. By counting the elements at each degree between 0 and 180, normal histograms were obtained to quantify population mean (μ) and standard deviations (σ) (Figure S8, Supporting Information). This was performed for junction bots at 5 D, 10 D, and 15 D (Figure S9, Supporting Information). Distribution of myotube orientation evolved from an almost uniform distribution at 5 D ($\sigma > 30$) to a normal distribution, plateauing by 15 D ($\sigma \approx 15$), as cues from stiffer fibrin matrix fibers directed alignment (Figure 7b). Furthermore, during tissue maturation, the mean of the orientation distribution approached 90°, aligned toward the direction of pillar actuation. To elucidate if there was a direct correlation between alignment and force production, the mean force per stroke was plotted against both the population mean, μ , and the standard deviation, σ , for three junction bots at 5 D, 10 D, and 15 D each. There were two possibilities. The first was that alignment played little role in general force production, but rather it was an effect of tissue maturation. The second was that either a net alignment of myotubes toward the direction of pillar actuation or a homogenous alignment which minimized cancellation of force vectors from misaligned myotube components leads to a larger force production.

The produced forces at different frequencies of stimulation did have, as expected, a positive relationship with μ , and a negative relationship with σ . However, there was no discernable trend with either. A positive linear relationship was observable when correlating force produced to the ratio of μ/σ (Figure S10, Supporting Information), and within a same day of measurement, force values consistently showed a positive

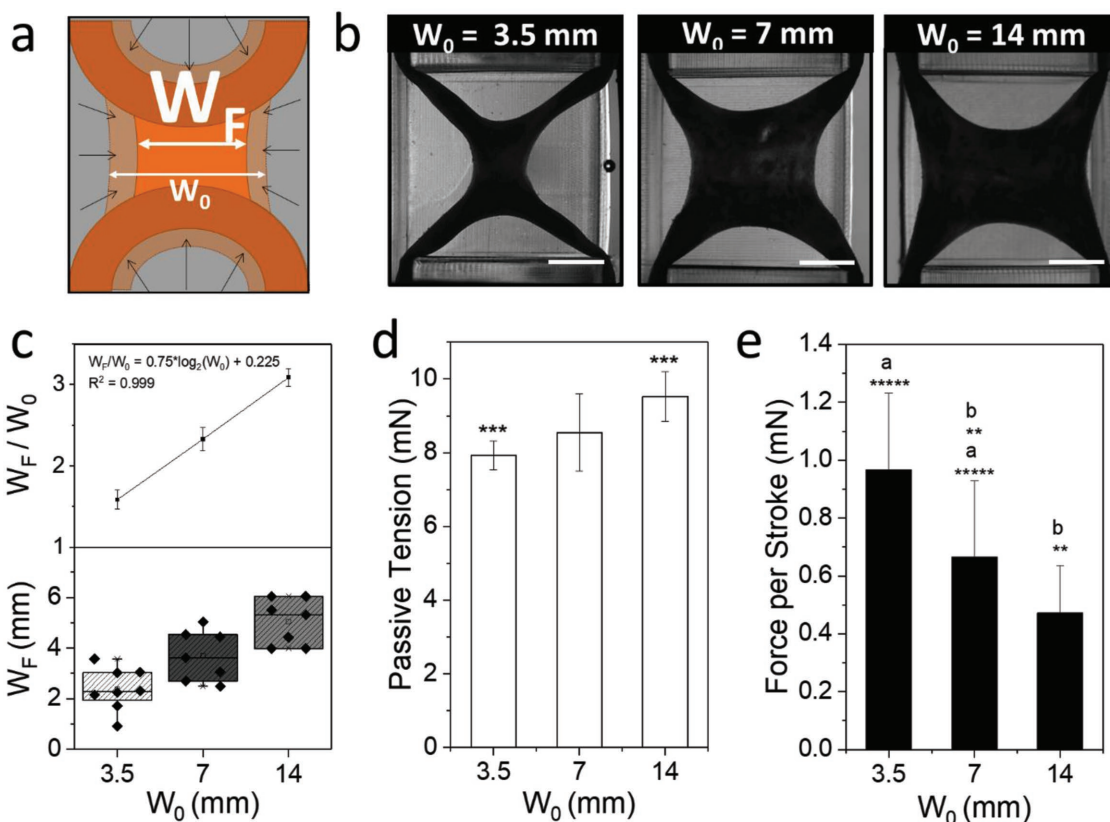


Figure 6. Force dependence to junction width. a) Representative image of the compaction process. b) Muscle after compaction from junction bots seeded on molds with varying trench width: 3.5 (top), 7 (middle), and 14 mm (bottom) (scale bar 2 mm). c) Compaction of biohybrid muscle, quantified by compaction ratio (W_F/W_0) (top; mean \pm SD, $n = 6$) and final width (W_F) (bottom; box plots range: 25/75 percentiles; $n = 6$). d) Passive force (mN) of mature junction bots (mean \pm SD, $n = 6$). e) Average active force peak from mature bots at varying seeding trench widths. (mean \pm SD, $n = 6$). (**p < 0.005; ***p < 0.0005, T-test).

linear trend in relation to the ratio. Interestingly, regardless of the frequency of stimulation, the slope of the linear fits seemed to be consistent at around $0.15 \pm 0.03 \text{ mN} \times (\mu/\sigma)^{-1}$ (Figure S11, Supporting Information).

Finally, force was also correlated with the alignment term of Equation (1) above at each day of the measurement (Figure 7c). As a physically relevant measurement of the influence of myotube alignment on actuation force, a normalized weighted average was defined as, $\overline{\chi}_\theta = \sum_{i=0}^{180} \omega'_i * \sin(\theta_i)$. Here, ω'_i is the value of the normalized magnitude component from the histograms for each respective degree of alignment in Figure 7b. These calculated values showed a very high linear relation with the measured force for each respective day, yet interestingly, also showed a clear dispersion for values across days. These empirical results confirm the relation between force and myotube alignment. This also seems to support our hypothesis regarding the effect of junction width to myotube alignment, with respect to force production as proposed in Figure 6 (Figure S11, Supporting Information). Nevertheless, the dispersion for force with respect to $\overline{\chi}_\theta$ across days of measurement would suggest that the model applies for a specific day of development as there might be other factors during tissue maturation that affect net contraction force. This is an opportunity for

future work to fully elucidate such parameters for a model that accommodates time as a variable in the development of force.

2.7. Predictive Model for Dynamics for Biological Machines

Another essential parameter to quantify during engineering of skeletal muscle-based biological machines is the dynamic functional output in response to the contraction force. Here, the skeletal muscle construct was fitted onto a PEGDA skeleton to achieve locomotion through a two-anchor gait. During stimulation, junction bots were placed with the pillars in contact with the substrate and tracked by a video camera as the cycling pillar displacement achieved net locomotion (Figure 8a; Movies S3 and S4, Supporting Information). Similarly, by setting the pillars of the computational junction bot model in “contact” with a simulated surface with a roughness similar to polystyrene, two-anchor gait locomotion was also successfully simulated. Our simulation also demonstrates the dynamic variation of kinetic friction coefficients required for forward “inch-worm” locomotion (Figure 8b; Movie S5, Supporting Information).^[7] It is relevant to clarify that the simulated displacement was achieved by setting an input through the modeled tissue, and the skeleton

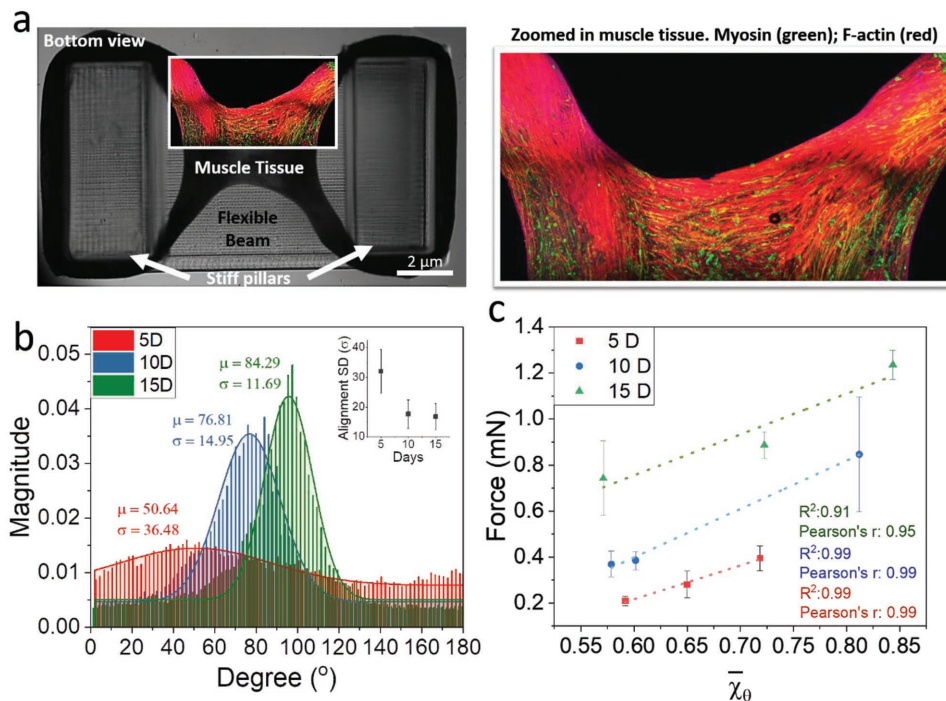


Figure 7. Force dependence to myotube alignment. a) Mature (15 D) junction bot showing myotube distribution and alignment through confocal microscopy. b) Representative histogram of magnitude of Fourier components versus degree of alignment for the myotubes at different days of maturation. The change of the dispersion of orientation of the myotubes was quantified with the standard deviation across the 5, 10, and 15 d (inlet; mean \pm SD, $n = 3$). c) Mean force produced per sample (mean \pm SD, $n = 4$) plotted against the degree score (angle of alignment (μ) divided by the standard deviation (σ)). Data points were linearly fitted ($P < 0.01$, one-way ANOVA).

would actuate as an output, thus resulting in an interaction with the simulated surface.

Both empirical and model-predicted position-time curves of junction bots depended strongly on stimulation frequency (Figure 8c), with the walking speed increasing with increasing stimulation frequency. While empirical results and model predictions matched well for 0.5 and 1 Hz stimulation frequencies, agreement was poorer for 2 and 4 Hz. This was not unexpected as simulating this slip-stick model of displacement is highly dependent on the initial state and, more importantly, the interplay between the forward and reverse friction coefficients of which the effects become more chaotic at higher frequencies. Therefore, we established that the high-accuracy of our computational model was limited to oscillation frequencies below 2 Hz (Figure 8b,c, shaded area). On the other hand, it is worth pointing out that this larger and higher-force producing biobot design was able to reach speeds $>0.5 \text{ mm s}^{-1}$ at 4 Hz (Figure 8d), corresponding to an approximately twofold increase from previous designs.^[6] This demonstrates the performance of these biological machines with respect to external stimuli as well as muscle geometry.

An analysis of work exercised on the pillars by the muscle tissue for junction bot showed no significant change between stimulation frequencies. However, when comparing with the work exercised during locomotion, which was parameterized as its efficiency, $\eta = \frac{\text{Work during locomotion}}{\text{Work on pillar}}$ (Figure 8d), there was a decrease from $0.71 \pm 0.21 \mu\text{J } \mu\text{J}^{-1}$ at 0.5 Hz to $0.46 \pm 0.02 \mu\text{J } \mu\text{J}^{-1}$ at 1 Hz, and then plateaued for higher

stimulation frequencies. This implies that, even though stimulating at 4 Hz can result in significantly higher speeds than at 0.5 Hz, the efficiency at 4 Hz being only $0.52 \pm 0.2 \mu\text{J } \mu\text{J}^{-1}$ implied higher slipping between the pillars and the substrate. This efficiency could be optimized by further treating pillar tips with surfactants or other fabrication processes to increase the friction coefficient. This would enable the engineering of biological machines to reach even higher speeds with decreased variability.

3. Conclusion

Tissue engineering has had a major focus of employing muscle cells as actuators capable of driving a large range of directed functionalities.^[40] Impressive breakthroughs have been achieved using self-contractile tissue, to engineer pumps and structures capable of locomotion.^[1,4,5,7,41] However, the ability to modulate contractions for controlled outputs and functions has made engineering of skeletal muscle biohybrid actuators a central focus of the field.^[16,20,42,43] Furthermore, skeletal muscle provides the possibility of engineering motor neuronal circuitry capable of controlling contractile output to a higher degree.

A critical part of advancing this field of study is to lay the foundation of principles that direct the engineering of next generation biological machines. To this purpose, the present work has developed a platform that links computational modeling to empirical validation for biological machines. This provides a proof of concept of the ability to start designing biohybrid

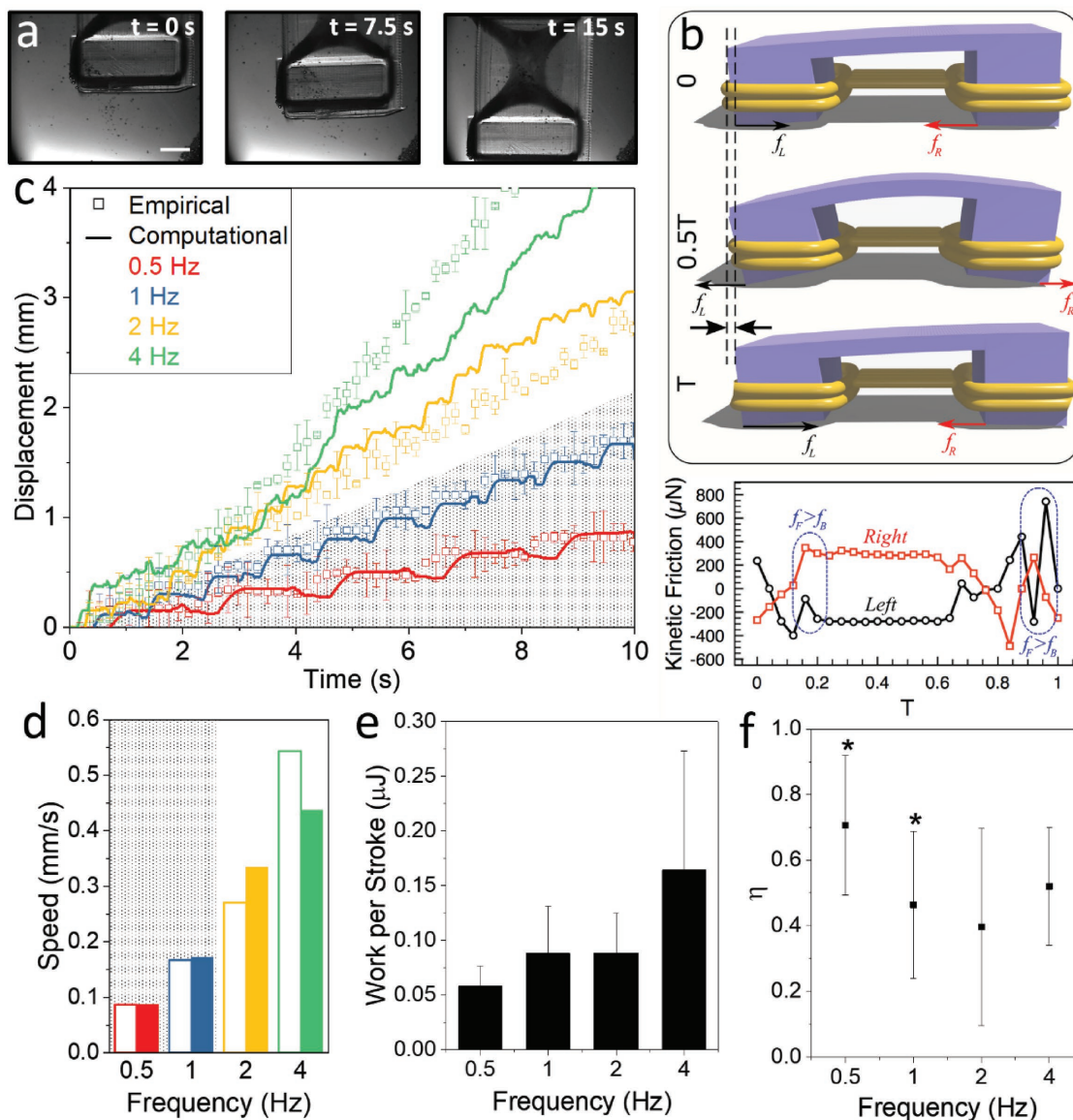


Figure 8. Functional output of junction bot. a) Snapshots of junction bot locomotion (scale bar: 2 mm). b) Simulated gait for one period of junction bot displacement by a two-anchor mechanism of locomotion (top). The kinetic friction force change for each leg with respect to the period (bottom). c) Displacement versus time for different stimulation frequencies (0.5, 1, 2, and 4 Hz). Points are experimental data and solid lines are modeled junction bots at same frequencies of stimulation. d) Speed of displacement between experimental (clear bars) and computational (solid) results for different frequencies of stimulation. e) Work per stroke calculated from bot displacement multiplied by the force measured for that respective junction bot at the corresponding stimulation frequency (mean \pm SD, $n = 3$). f) Efficiency (η) plotted against each stimulation frequency (mean \pm SD, $n = 3$). Efficiency was defined as $\eta = \frac{\text{Work during locomotion}}{\text{Work on pillar}}$ ($*p < 0.05$).

actuators with more complex geometries and targeted force outputs, which would result in the ability to engineer a wider range of function-specific performances. Here, we employed this concrete approach to intelligently increase the force output of autonomous biohybrid skeletal muscle biobots from $\approx 200\text{ }\mu\text{N}$ to $\approx 1.2\text{ mN}$ to actuate on a PEGDA scaffold that was twice as large as previous designs. By differentiating myoblasts on high stiffness substrates, versus 3D differentiation, their length was increased 1.5-fold and shown that these can still be effectively engrafted in a 3D construct without loss of viability. This length increase caused a force increase from each individual myotube

actuator within the tissue, thus resulting in a net force increase from the entire structure. This length improvement could be further extended by differentiating myoblasts in groove-patterned substrates or the use of high-Connexin 43-expressing myoblasts.^[44,45]

Utilizing the computational model, we designed a fitting larger muscle structure by targeting and optimizing concrete design parameters while addressing the nutrient diffusion-based thickness limit by designing a new mold geometry. This increase of geometry of actuating muscle served to further increase the force, where the structures were enlarged from

6 mm (for its longest dimension) to 1.3 cm. It was further coupled with a walking skeleton structure designed to handle the scaled force. This work also aimed to characterize empirical factors in an effort to validate the proposed design criteria, primarily quantifying force to be correlated with the degree of alignment of the individual myotubes.

The resulting design could have the additional benefit of facilitating the introduction of other constructs, such as motor neuronal structures, by providing a physical platform on where to place such tissue. This is particularly advantageous since achieving adhesion in these types of suspended structures poses a real obstacle during modular approaches to multi-phenotypical tissue engineering.^[46] Theoretically, a bundle of synthetic motor neuronal circuits that have been engineered to contain central pattern generators could be modularly placed on the junction for adherence, innervation, and neuronal control of the structure.

We also developed a computational model that was able to simulate the dynamics of the muscle and its interaction with the skeleton. This model showed a high correlation with empirical force data, and, more importantly, effectively predicted the degree of the functional output, e.g., locomotion, with high accuracy. This could therefore be a great aid in the design of future biological machines that are able to exhibit more complex behaviors and achieve precise tasks with a high degree of control. Using this modeling approach, we can now computationally explore new skeleton designs that incorporate targeted modifications to critical structures and dimensions such as the beam thickness, pillar length, skeleton mass, etc., to achieve a specific metrics of performance and functionality.

4. Experimental Section

Simulation and Modeling: Muscles are considered as bundles of quasi 1D filaments, which can have large deformations in multiple directions. To capture this physics, a numerical method^[27] based on Cosserat rod theory^[47] is implemented for the muscle simulation, which solves the dynamic and deformative problems of soft rods with large deflections. For the sake of modeling the entire system with one set of equations, same theory is leveraged for modeling the skeleton. Thus, in simulation, an assembly of 1D rods with rectangular cross-sections constructs the skeleton, whose mechanical properties are essentially preserved. Detailed explanations are presented in Note S1 (Supporting Information).

Interactions within multiple filaments, and between filaments and environments, are also included in the simulation. Repulsive forces are generated when the muscle is in contact with the pillars, eliminating all the interpenetrations. Formulations and implementations of the interaction schemes are also included in Note S1 (Supporting Information). Coulomb friction model is applied at the surface between the pillars and the ground, while hydrodynamic forces are applied to the entire body.^[27]

2D Myoblast Culture and Differentiation: C2C12 murine myoblasts were seeded at 0.3e6 cells per well in a cell culture six-well plate and cultured in muscle growth media (mGM) consisting of Dulbecco's modified Eagle medium (DMEM) with L-glutamine and sodium pyruvate (DMEM, Corning Cellgro) supplemented with 10% fetal bovine serum (Lonza), 1% L-glutamine, and 1% penicillin-streptomycin (Cellgro Mediatech, Inc.). When cultures reached 80–90% confluence at ≈2–3 d, media was switched to muscle differentiation media (mDM). Differentiation media consisted of DMEM supplemented with 10% horse serum (Lonza),

1% L-glutamine, and 1% penicillin-streptomycin. 2D differentiation was continued for 5 d, changing media daily. All cultures were kept in incubators at 37 °C and 5% CO₂.

Formation of 3D Skeletal Muscle Tissue: The construction of myoblast formed skeletal muscle tissue followed previously published protocol.^[6] In summary, each muscle ring was formed from a solution of 0.5 × 10⁶ myoblasts mixed with 30% Matrigel (Corning), 4 mg mL⁻¹ fibrinogen (Sigma-Aldrich), and 1 U per mg⁻¹ fibrinogen of thrombin (Sigma-Aldrich), and mGM was added for a total of 100 μL of solution. Each cell-fibrin solution was dispensed to a PEGDA mold and permitted to compact for 3 d in mGM before being switched to mDM supplemented with 1× aminoproic acid (ACA, Sigma-Aldrich).

Myotube formed skeletal muscle tissue rings were formed analogously to MB rings. Differentiated 2D myotubes were trypsinized with TrypLE and delicately triturated mechanically to achieve a single cell suspension without breaking the myotubes. Half the cell contents of a single well were used for a single MT ring by using the same ECM–fibrin hydrogel composition used for MB rings.

Design and 3D Printing of Mold and Skeleton Structures: Biobot ring molds and skeletons were 3D printed using a customized SLA (250/50, 3D Systems). Ring molds were fabricated using 20% w/v PEGDMA M_w 1000 g mol⁻¹ and skeletons were fabricated from 20% w/v PEGDA M_w 700 g mol⁻¹. Both solutions also contained 0.5% w/v of the photoinitiator Irgacure 2959 (Ciba). Fabricated parts were sterilized in 70% EtOH for 1 h and then stored in Phosphate-buffered saline (PBS) prior to use.

Electric Stimulation: A waveform generator was used to depolarize muscle tissue by connecting to a AD797 inverting amplifier. Square pulses were converted into biphasic pulses by connecting a capacitor C in series turning the system into an RC circuit. This was done to avoid electrolysis of the cells. Two parallel platinum wires were held in place by a square acrylic well that could be fitted into the 6-well plates where the junction bots were placed for measurement. Each wire was connected to the electrode contacts to run an electrical current perpendicular to the muscle from the cathode to the ground.

Measurement of Force and Locomotion: Muscle actuation was recorded through a stereomicroscope (MZ FL III, Leica Microsystems) by using a digital microscope camera (Flex, SPOT Imaging Solutions) to image junction bots with pillars facing the camera at a frame rate of 6 f s⁻¹. The bending of the junction bot's beam was correlated to the pillar deflection in response to the contraction of the muscle. This displacement was measured in ImageJ (National Institutes of Health). Passive tension force was then calculated using the Euler–Bernoulli beam-bending theory

$$P = k * \delta_{\max}; \quad \text{for } k = \frac{8EI}{L^2l} \quad (3)$$

where δ_{\max} is the measured deflection displacement. The other constant values were calculated for the beam, where I is the moment of inertia, L is the longitudinal dimension, and l is the moment arm from the point of applied force of the tissue to the beam. E represents the Young's Modulus, which was previously measured to be 319 kPa, for the chosen fabrication parameters. Stimulated tension force was calculated with the same model, using the transient deflections displacements produced by the contractile force of the skeletal muscle tissue under electrical stimulation at varying frequencies.

Immunofluorescence Imaging: Prior to staining, muscle tissue was rinsed with PBS and fixed in 4% (v v⁻¹) of paraformaldehyde for 20 min on the skeleton structure to conserve the tissue structure during steady state. Samples were then washed with PBS three times and removed from the structure by cutting the PEGDA pillars. Triton-X was diluted to 0.25% (v v⁻¹) and used to permeabilize the tissue membrane for 20 min. After washing with PBS, samples were blocked and stored in 1% (w v⁻¹) bovine serum albumin (Sigma-Aldrich) at 4 °C until ready to stain (no more than two weeks).

Cell membrane was immunolabeled with a 1:200 dilution of 488-conjugated antibody reactive to F-actin, by incubating overnight at

4 °C. The primary antibodies, mouse anti-myosin heavy chain (MF-20) and rabbit anti- α -actinin, were used to stain for myosin and the sarcomere, respectively, at a 1:500 dilution. Tissues were incubated with the primary antibodies for 12 h at 4 °C. Samples were then washed three times before staining with secondary antibodies. AlexaFluor-647 anti-mouse (ThermoFisher) and AlexaFluor-633 anti-rabbit (ThermoFisher) were used to stain MF-20 and α -actinin primary antibodies, respectively, and incubated for 2 h at room temperature.

To be able to image 3D tissue without distorting the internal cellular structure, stained samples were fitted into a custom-made polydimethylsiloxane (PDMS) mold, embedded in 1% agarose, and covered with a coverslip to ensure the agarose surface would be even. These molds were plasma bonded to a microscope slide. For imaging, the slides were flipped with the agarose facing the objective for high resolution confocal imaging.

Alignment Quantification: The orientation of myotubes was quantified using the Directionality plugin for ImageJ which uses Fourier component analysis, which computes a histogram which counts the amount of myotubes in a given direction, numbered as degrees.^[48] Because myotubes show a preferred direction, the calculated histogram shows a singular peak at that orientation. A Gaussian fit is calculated from the highest peak.

Fluorescent imaging was used to visualize the myotube membranes on the junction stained with conjugated F-actin. Images were uploaded to ImageJ and cropped to include only the region of the muscle junction. Fourier power spectra was later computed using the Directionality plugin. All samples showed a goodness of fit above 0.9.

Myogenic Maturity Assays: Biobot muscle rings were rinsed in PBS, snap frozen in liquid nitrogen for 5 min, and stored at -80 °C. To analyze muscle creatine kinase activity, samples were thawed at room temperature. The muscle tissue was broken up using a pair of microscissors, and 300 μ L of RIPA buffer (Thermo Scientific) was added to the sample. Samples were vortexed, then rocked at 4 °C for 30 min to break apart the tissue. Samples were then sonicated at a power of 1 W for \approx 10 s, or until no visible pieces of tissue remained. The samples were then centrifuged for 15 min at 14 000 G and 50 μ L of supernatant was mixed with 1 mL of warm creatine kinase working reagent, prepared according to the supplier's instructions (liquid creatine kinase reagent set, Pointe Scientific Inc). 100 μ L of the mixture was then transferred to a 96 well plate, which was incubated at room temperature for 2 min. The plate was read at 340 nm, with seven readings taken at 1 min intervals at 37 °C. MCK activity in U/L was calculated from the change in absorbance with time.

Viability Assay: The MTS assay working reagent was prepared by combining MTS solution (CellTiter 96 AQueous One Solution Cell Proliferation Assay, Promega) with warm DMEM (without phenol red) in a 1:5 ratio. Muscle rings were rinsed in PBS, placed in individual wells of a 24 well plate, and immersed in 360 μ L of MTS working reagent. The reaction proceeded in the dark for 4 h at 37 °C. Absorbance at 490 nm was used to measure metabolic activity, and thus cell viability.

Supporting Information

Supporting Information is available from the Wiley Online Library or from the author.

Acknowledgements

The authors thank Dr. Ritu Raman from Massachusetts Institute of Technology for technical discussions, and Dr. Mayandi Sivaguru from University of Illinois, Urbana-Champaign for assistance with fluorescence imaging. This work was funded by National Science Foundation (NSF) Science and Technology Center Emergent Behavior of Integrated Cellular Systems (EBICS) Grant CBET0939511, and in part supported from DTRA interagency agreement 160298. G.J.P.-D. was supported by National Science Foundation Graduate Research Fellowship Program under

Grant Number DGE-1144245. The authors thank the Blue Waters project (OCI-0725070, ACI-1238993), a joint effort of the University of Illinois at Urbana-Champaign and its National Center for Supercomputing Applications, for partial support (M.G.).

Note: The Acknowledgements section was revised on June 11, 2018, after initial publication online.

Conflict of Interest

The authors declare no conflict of interest.

Keywords

biohybrid robots, biological machines, PEGDA scaffolds, skeletal muscles, tissue modeling

Received: February 11, 2018

Revised: March 13, 2018

Published online: April 23, 2018

- [1] B. J. Williams, S. V. Anand, J. Rajagopalan, M. T. A. Saif, *Nat. Commun.* **2014**, *5*, 3081.
- [2] R. D. Kamm, R. Bashir, *Ann. Biomed. Eng.* **2014**, *42*, 445.
- [3] R. M. Duffy, A. W. Feinberg, *Wiley Interdiscip. Rev.: Nanomed. Nanobiotechnol.* **2014**, *6*, 178.
- [4] J. C. Nawroth, H. Lee, A. W. Feinberg, C. M. Ripplinger, M. L. McCain, A. Grosberg, J. O. Dabiri, K. K. Parker, *Nat. Biotechnol.* **2012**, *30*, 792.
- [5] B. McInroe, H. C. Astley, C. Gong, S. M. Kawano, P. E. Schiebel, J. M. Rieser, H. Choset, R. W. Blob, D. I. Goldman, *Science* **2016**, *353*, 154.
- [6] C. Cvetkovic, R. Raman, V. Chan, B. J. Williams, M. Tolish, P. Bajaj, M. S. Sakar, H. H. Asada, M. T. A. Saif, R. Bashir, *Proc. Natl. Acad. Sci. USA* **2014**, *111*, 10125.
- [7] V. Chan, K. Park, M. B. Collens, H. Kong, T. A. Saif, R. Bashir, *Sci. Rep.* **2012**, *2*, 857.
- [8] S. Park, M. Gazzola, K. Park, S. Park, V. Di Santo, E. Blevins, J. Lind, P. Campbell, S. Dauth, A. Capulli, F. Pasqualini, S. Ahn, A. Cho, H. Yuan, B. Maoz, R. Vijaykumar, J. Choi, K. Deisseroth, G. Lauder, L. Mahadevan, K. Parker, *Phototactic guidance of a tissue-engineered soft-robotic ray*, *Science*, **2016**, *353*, 158.
- [9] P. Bajaj, R. M. Schweller, A. Khademhosseini, J. L. West, R. Bashir, *Annu. Rev. Biomed. Eng.* **2014**, *16*, 247.
- [10] W. Bian, B. Liau, N. Badie, N. Bursac, *Nat. Protoc.* **2009**, *4*, 1522.
- [11] V. Chan, M. B. Collens, J. H. Jeong, K. Park, H. Kong, R. Bashir, *Virtual Phys. Prototyping* **2012**, *7*, 219.
- [12] M. P. Lutolf, J. A. Hubbell, *Nat. Biotechnol.* **2005**, *23*, 47.
- [13] M. Calisti, G. Picardi, C. Laschi, *J. R. Soc. Interface* **2017**, *14*, 20170101.
- [14] J. L. Drury, D. J. Mooney, *Biomaterials* **2003**, *24*, 4337.
- [15] V. Chan, J. H. Jeong, P. Bajaj, M. Collens, T. Saif, H. Kong, R. Bashir, *Lab Chip* **2012**, *12*, 88.
- [16] M. S. Sakar, D. Neal, T. Boudou, M. A. Borochin, Y. Li, R. Weiss, R. D. Kamm, C. S. Chen, H. H. Asada, *Lab Chip* **2012**, *12*, 4976.
- [17] J. H. Jeong, V. Chan, C. Cha, P. Zorlutuna, C. Dyck, K. J. Hsia, R. Bashir, H. Kong, *Adv. Mater.* **2012**, *24*, 58.
- [18] C. Cvetkovic, M. C. Ferrall-Fairbanks, E. Ko, L. Grant, H. Kong, M. O. Platt, R. Bashir, *Sci. Rep.* **2017**, *7*, 3775.
- [19] T. Shimizu, M. Yamato, Y. Isoi, T. Akutsu, T. Setomaru, K. Abe, A. Kikuchi, M. Umezawa, T. Okano, *Circ. Res.* **2002**, *90*, e40.
- [20] R. Raman, C. Cvetkovic, R. Bashir, *Nat. Protoc.* **2017**, *12*, 519.

- [21] C. S. Cheng, B. N. Davis, L. Madden, N. Bursac, G. A. Truskey, *Exp. Biol. Med.* **2014**, 239, 1203.
- [22] M. Linari, E. Brunello, M. Reconditi, L. Fusi, M. Caremani, T. Narayanan, G. Piazza, V. Lombardi, M. Irving, *Nature* **2015**, 528, 276.
- [23] R. H. Fitts, K. S. McDonald, J. M. Schluter, *J. Biomech.* **1991**, 24, 111.
- [24] S. Gehlert, F. Suhr, K. Gutsche, L. Willkomm, J. Kern, D. Jacko, A. Knicker, T. Schiffer, H. Wackerhage, W. Bloch, *Pflügers Arch.* **2015**, 467, 1343.
- [25] W. Herzog, T. R. Leonard, *J. Exp. Biol.* **2002**, 205, 1275.
- [26] R. Raman, C. Cvetkovic, S. G. M. Uzel, R. J. Platt, P. Sengupta, R. D. Kamm, R. Bashir, *Proc. Natl. Acad. Sci. USA* **2016**, 113, 3497.
- [27] M. Gazzola, L. Dudte, A. G. McCormick, L. Mahadevan, **2016**, arXiv:1607.00430.
- [28] S. L. Rowe, S. Lee, J. P. Stegemann, *Acta Biomater.* **2007**, 3, 59.
- [29] D. E. Rassier, B. R. MacIntosh, W. Herzog, *J. Appl. Physiol.* **1999**, 86, 1445.
- [30] M. Lovett, K. Lee, A. Edwards, D. L. Kaplan, *Tissue Eng., Part B* **2009**, 15, 353.
- [31] R. N. Palchesko, L. Zhang, Y. Sun, A. W. Feinberg, *PLoS One* **2012**, 7, e51499.
- [32] A. J. Engler, M. A. Griffin, S. Sen, C. G. Bönnemann, H. L. Sweeney, D. E. Discher, *J. Cell Biol.* **2004**, 166, 877.
- [33] H. Duong, B. Wu, B. Tawil, *Tissue Eng., Part A* **2009**, 15, 1865.
- [34] J. E. Johnson, B. J. Wold, S. D. Hauschka, *Mol. Cell. Biol.* **1989**, 9, 3393.
- [35] J. Rouwkema, B. F. J. M. Koopman, C. A. V. Blitterswijk, W. J. A. Dhert, J. Malda, *Biotechnol. Genet. Eng. Rev.* **2009**, 26, 163.
- [36] R. Horowitz, E. S. Kempner, M. E. Bisher, R. J. Podolsky, *Nature* **1986**, 323, 160.
- [37] L. Wang, Y. Li, B. Chen, S. Liu, M. Li, L. Zheng, P. Wang, T. J. Lu, F. Xu, *ACS Appl. Mater. Interfaces* **2015**, 7, 15088.
- [38] A. Tondon, R. Kaunas, *PLoS One* **2014**, 9, e89592.
- [39] H. Aubin, J. W. Nichol, C. B. Hutson, H. Bae, A. L. Sieminski, D. M. Cropek, P. Akhyari, A. Khademhosseini, *Biomaterials* **2010**, 31, 6941.
- [40] L. Ricotti, B. Trimmer, A. W. Feinberg, R. Raman, K. K. Parker, R. Bashir, M. Sitti, S. Martel, P. Dario, A. Menciassi, *Sci. Rob.* **2017**, 2, eaaq0495.
- [41] Y. Tanaka, K. Morishima, T. Shimizu, A. Kikuchi, M. Yamato, T. Okano, T. Kitamori, *Lab Chip* **2006**, 6, 362.
- [42] K. Shimizu, H. Sasaki, H. Hida, H. Fujita, K. Obinata, M. Shikida, E. Nagamori, *Biomed. Microdevices* **2010**, 12, 247.
- [43] V. A. Webster, E. L. Hawley, O. Akkus, H. J. Chiel, R. D. Quinn, *Bioinspiration Biomimetics* **2016**, 11, 036012.
- [44] M. Peckham, *J. Microsc.* **2008**, 231, 486.
- [45] C. C. Yuan, K. J. Ma, K. C. Li, H. H. Chien, H. E. Lu, C. P. Tseng, S. M. Hwang, *Micro Nano Lett.* **2013**, 8, 440.
- [46] Y. Morimoto, M. Kato-Negishi, H. Onoe, S. Takeuchi, *Biomaterials* **2013**, 34, 9413.
- [47] E. Cosserat, F. Cosserat, *Théorie des Corps Déformables*, Librairie Scientifique (Ed.: A. Hermann) et Fils, Paris **1909**.
- [48] Z.-Q. Liu, *Appl. Opt.* **1991**, 30, 1369.